polymer papers

NEW-TPI thermoplastic polyimide: thermal analysis and small-angle X-ray scattering

Peter P. Huo*, Jerome B. Friler† and Peggy Cebe‡
Department of Materials Science and Engineering, Massachusetts Institute of Technology, Cambridge, MA 02139, USA
(Received 29 July 1992; revised 8 February 1993)

Isothermal cold crystallization of the thermoplastic polyimide NEW-TPI has been investigated from 300 to 360°C. The fastest crystallization took place at 330°C where the time to maximum exothermic heat flow was 148 s. A single Avrami exponent could be used to describe the bulk crystallization kinetics for degrees of conversion from 0.02 up to 0.95, indicating that most crystallization takes place at the growth front by a single mechanism, nearly up to the completion of crystallization. The Avrami exponent is 3.5 for $T_c < 330$°C, and decreases as T_c increases. A regime II to III transition is indicated by a slope change seen in $\ln(1/t_{1/2}) + U/R(T - T_\infty)$ vs. $1/T\Delta Tf$. These results indicate that NEW-TPI cold crystallization can be modelled according to heterogeneous nucleation and three-dimensional crystal growth. From T_m vs. T_c analysis, the infinite-crystal melting point of NEW-TPI is estimated to be 400°C. With regard to the glass transition, T_g was affected by cold crystallization in a systematic but minor way. The heat-capacity increment of semicrystalline NEW-TPI at T_g shows a small negative deviation from that predicted on the basis of the degree of crystallinity. The absence of secondary crystallization processes has been used to explain the different glass transition behaviour and small negative heat-capacity deviation in NEW-TPI. Real-time small-angle X-ray scattering (SAXS) was used to monitor the structure change as a function of cold crystallization time at 300°C. Systematic change of long period, lamellar thickness, invariant and volume fraction of crystallinity were obtained from the one-dimensional electron density correlation function analysis. At $T_c = 300$°C, lamellar thickness as a function of t_c ranges from 37 to 52 Å, or about 1.5–2.0 times the monomer repeat unit. The thickness of the interphase region was determined from SAXS to be about 17 Å independent of cold crystallization time at 300°C.

(Keywords: thermoplastic polyimide; thermal analysis; small-angle X-ray scattering)

INTRODUCTION

Aromatic polyimides have been widely used in applications requiring insulating properties under harsh service requirements. They possess a unique property combination in which outstanding thermal stability and radiation and solvent resistance are coupled to excellent mechanical, electrical and adhesive properties over a wide range of temperatures[1–7]. Applications for polyimide films include electronic packaging for printed circuits, insulation for lead wire, control cable and aerospace wire where weight and space savings are essential. Aromatic polyimides such as PMDA–ODA (from pyromellitic dianhydride with 4,4′-oxydianiline) (chemical analogue of DuPont's Kapton) and BTDA–ODA (benzophenone tetracarboxylic dianhydride with 4,4′-oxydianiline) are processed and used as amorphous materials. They are usually coated as varnish, or spun cast as thin films, from the poly(amic acid) precursor, and then thermally imidized *in situ*. The rigidity of the chains results in high glass transition temperatures and often leads to a decomposition temperature that is reached before the crystal melting point. This makes them extremely difficult to melt-process and crystallize.

Recent efforts have been directed towards producing polyimides that are crystallizable thermoplastics. The choice of synthetic methods used to lower the transition temperatures includes the incorporation of substitutes onto the aromatic rings and the addition of more flexible units and/or *meta* linkages into the polymer backbone[2–6]. The latter route was used to synthesize the polyimide known as NEW-TPI (Mitsui Toatsu Chemical Co.)[8], which is capable of crystallizing, and yet maintains very high transition temperatures. The glass transition of NEW-TPI is about 250°C and the crystal melting point determined from differential scanning calorimetry (d.s.c.) is near 380°C[8–13]. NEW-TPI is a very promising material in terms of its superior mechanical properties, high-temperature stability, solvent resistance and melt processability[8–13]. The chemical structure of NEW-TPI has been reported previously[10,11,13], and consists of PMDA and a diamine comprising phenyl–ether and phenyl–phenyl units.

So far, there have been only very limited studies reported on NEW-TPI. Sakaitani *et al.*[14] determined the lattice parameters using X-ray diffraction of NEW-TPI fibres. Takahashi and coworkers studied thin films by transmission electron microscopy and determined that spherulites were present[15]. Sasuga reported the effects of electron beam irradiation on the mechanical properties of NEW-TPI[12]. We have reported results on the

* Present address: W. R. Grace Corp., Columbia, MD, USA
† Present address: Mitsui Toatsu Chemical Co., Tokyo, Japan
‡ To whom correspondence should be addressed

0032-3861/93/214387-12

development of crystallinity in powder, pellets and film[10], non-isothermal crystallization[10], and dielectric and dynamic mechanical relaxation behaviour[11,16].

In our prior dielectric relaxation study[11], we observed a very different amorphous phase relaxation behaviour of NEW-TPI compared with other high-performance polymers that we studied[17,18]. The rigid portion of the amorphous phase identified from the thermal analysis of the heat-capacity increment[17–28] constitutes a relatively small fraction in NEW-TPI, and it relaxes upon heating within a narrow temperature window of about 20°C above the glass transition temperature. In this work, we report our results on the isothermal cold crystallization of NEW-TPI. We have studied the crystallization kinetics, glass transition and melting behaviour, and structure of semicrystalline NEW-TPI through a combination of thermal analyses and real-time small-angle X-ray scattering. Crystallization behaviour is compared to other engineering thermoplastics, poly(ethylene terephthalate) (PET)[29–33], poly(ether ether ketone) (PEEK)[34–36] and poly(phenylene sulfide) (PPS)[37–42].

EXPERIMENTAL

NEW-TPI film (Mitsui Toatsu Regulus™) was received from Foster Miller Inc. processed by extrusion from pellets (Aurum™). The as-received NEW-TPI film is a transparent amorphous film as seen by wide-angle X-ray scattering (WAXS) and d.s.c. As-received film was dried in a Mettler hot stage at 150°C for 20 h, then relaxed at 260°C for 20 h[8,10] prior to testing. This treatment was used to prepare all films used in this study. Therefore, we will hereafter refer to these treated films either as amorphous, or according to their subsequent crystallization history.

A Perkin–Elmer DSC-4 was used to study the cold crystallization kinetics of NEW-TPI as a function of crystallization temperature, T_c, or time, t_c. The amorphous samples were heated from below T_g to T_c, at a heating rate of 200°C min^{-1}, and held at T_c for measurement of exothermic heat flow until the completion of crystallization. The cold crystallization temperatures were chosen to be from 300 to 360°C. Because of the relatively slow cold crystallization kinetics of NEW-TPI, we were able successfully to heat the samples to the highest crystallization temperatures without crystallization occurring at lower temperature.

As a function of either T_c or t_c, the melting peak temperature, glass transition temperature, heat-capacity step at T_g and ultimate degree of crystallinity were measured. Indium was used as the temperature calibrator, and a sapphire standard was used for heat-capacity measurements. For the crystallization time dependence study, we chose 300°C as the cold crystallization temperature, and varied t_c. Degree of crystallinity, χ_c, was determined from endotherm area, using 33.3 cal g^{-1} as the heat of fusion of perfect crystalline NEW-TPI[8]. The mobile, or liquid-like, amorphous fraction, χ_a, refers to the portion of the amorphous phase contributing to the heat-capacity increment at T_g during normal d.s.c. scanning at 20°C min^{-1}. The evaluation of χ_a was done in the manner described previously for PPS and PEEK[17–19,27,28]. The rigid amorphous fraction, χ_{ra}, was determined from[17–28]:

$$\chi_{ra} = 1 - \chi_a - \chi_c \quad (1)$$

Real-time small-angle X-ray scattering (SAXS) experiments were done in transmission mode at the Brookhaven National Synchrotron Light Source, utilizing a high-intensity source of X-ray radiation (1.54 Å). The system was equipped with a Braun one-dimensional position-sensitive detector. For SAXS, the sample-to-detector distance is 125 cm and the beam profile at the detector was treated according to pinhole geometry. The sample was inserted into a hot stage, which was already equilibrated at the crystallization temperature, and the SAXS intensity was measured in real time. SAXS intensity was corrected in the following way. First, background was subtracted from the raw data. The slope of Is^4 vs. s^4 (where s is the scattering vector, $s = 2\sin\theta/\lambda$) was used to obtain the diffraction intensity contribution from thermal density fluctuations, I_f. Here, we assume that the intensity from the thermal density fluctuations is a constant for all s. After subtraction of I_f, the corrected intensity, I_{corr}, is used for quantitative analysis.

RESULTS AND DISCUSSION

Cold crystallization kinetics

In *Figure 1*, we present heat flow, dQ/dt, vs. crystallization time during isothermal cold crystallization at several temperatures. These curves do not show the induction time for initiation of heat flow. In all cases, the d.s.c. had equilibrated at T_c before any exothermic heat flow was observed. The thermograms show a typical crystallization exothermic peak, but the curve shape is unusual in that it is very symmetric, compared for example to poly(ethylene terephthalate) (PET)[29–33], poly(ether ether ketone) (PEEK)[34–36] and poly(phenylene sulfide) (PPS)[37–42], all of which have a long period of heat flow beyond the exothermic maximum, which is usually attributed to secondary crystallization processes. The time to reach 50% partial crystallinity, $t_{1/2}$, is an indicator of the kinetics of the crystallization process and is listed in *Table 1*. The *fastest* crystallization time we observed was $t_{1/2} = 148$ s at $T_c = 330$°C. A plot of $t_{1/2}$ as a function of T_c is shown by symbols in *Figure 2*. The curve through the data represents the best fit to a second-order polynomial and suggests that the fastest crystallization for NEW-TPI occurs near 327°C. We shall

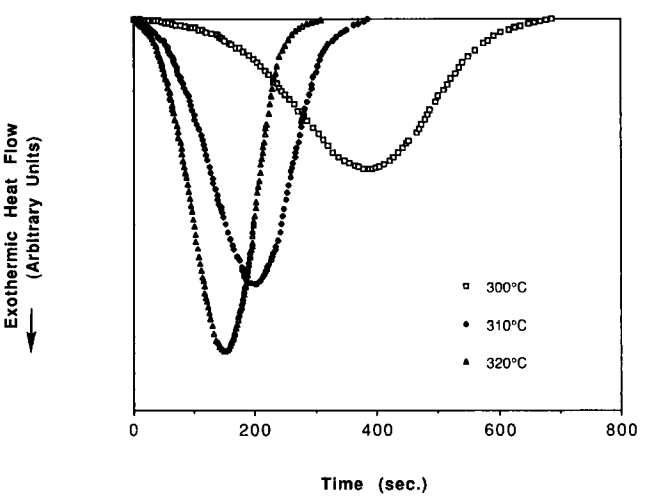

Figure 1 Exothermic heat flow vs. time for isothermal cold crystallization of NEW-TPI at the crystallization temperatures indicated

Table 1 Time to maximum heat flow and Avrami parameters for NEW-TPI cold crystallized at the indicated temperatures

Crystallization temp. (°C)	$t_{1/2}$ (s)[a]	t_c (s)[b]	n	$\log[K(s^{-n})]$
300	377	715	3.59	−9.41
310	200	390	3.49	−8.19
320	152	304	3.55	−7.94
330	148	285	3.52	−7.77
340	182	357	3.31	−7.51
350	280	519	2.97	−6.89
360	660	1202	2.83	−7.34

[a] $t_{1/2}$ is the time to 0.50 partial crystallinity
[b] t_c is the time to completion of crystallization

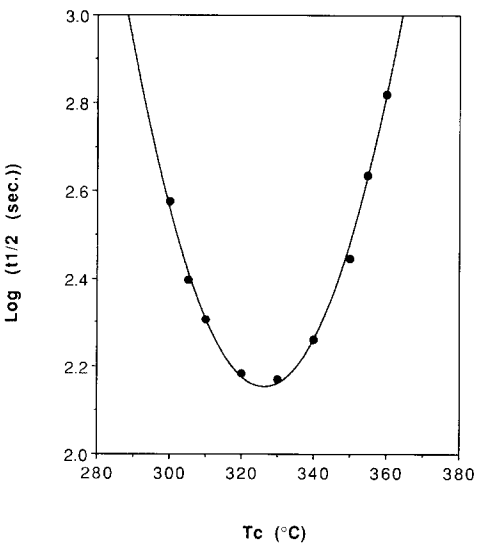

Figure 2 Log($t_{1/2}$) vs. cold crystallization temperature for NEW-TPI

designate as T'_c the temperature (here, 327°C) at which the growth rate is fastest. Over the 60°C temperature range we studied, time to maximum heat flow is of the order of several minutes, as shown in *Table 1*.

NEW-TPI has relatively slow kinetics, compared with other high-performance thermoplastic polymers such as PET[29–33], PPS[37–42] or PEEK[34–36], which have measured crystallization times $t_{1/2}$ of the order of seconds. Additional evidence for the slow cold crystallization kinetics has been presented in our previous report of dynamic mechanical relaxation and dielectric relaxation experiments[11,16]. NEW-TPI has a relatively small crystallization temperature window, which is defined as the temperature range between the glass transition temperature (~250°C) and infinite-crystal melting point (shown in this work to be 400°C). For NEW-TPI, this window is only about 150°C, much smaller than for PET (200°C)[29–33], PPS (220°C)[37–42] or PEEK (250°C)[34–36]. Also, we find that the final crystallinity is fairly low, below 0.30 by weight for any cold crystallization temperature. These results are quite consistent with our prior study on the non-isothermal crystallization of NEW-TPI[10].

The time development of relative crystallinity, a, is shown in *Figure 3a*. Here we plot a vs. t where the relative crystallinity is given by:

$$a = \frac{X_c(t)}{X_c(\infty)} \tag{2}$$

and $X_c(t)$ and $X_c(\infty)$ are the crystallinity at time t and at the completion of crystallization, respectively. The Avrami equation[43,44] has been widely used to describe the overall rate of bulk crystallization according to which a is written as:

$$a = 1 - \exp(-Kt^n) \tag{3}$$

where n is the Avrami exponent, which depends on the type of nucleation and crystal growth geometry, and K is a constant only dependent on T_c. K is related to the linear growth rate G by $K \sim G^n$.

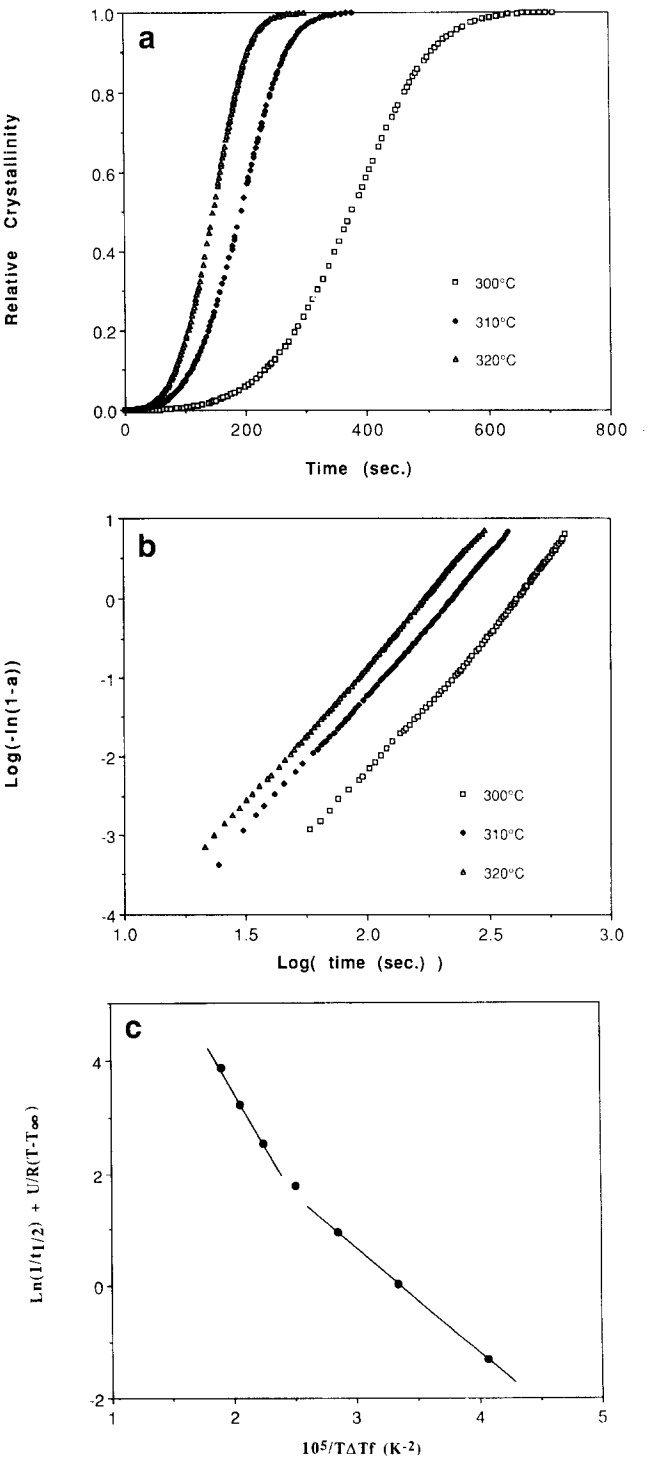

Figure 3 Isothermal cold crystallization of NEW-TPI: (a) relative crystallinity, a, as a function of crystallization time; (b) $\log[-\ln(1-a)]$ vs. $\log(t)$; and (c) $\ln(1/t_{1/2}) + U/R(T-T_\infty)$ vs. $1/T\Delta Tf$

To obtain the Avrami constant n and K, we plot $\log[-\ln(1-a)]$ vs. $\log(t)$, the slope of which is the Avrami exponent, n, and the intercept is the constant, $\log(K)$. Several examples are shown in *Figure 3b*, where it should be noted that the straight-line relationship persists from about 0.01–0.02 relative crystallinity nearly until the completion of the crystallization process. Below about 0.01–0.02 relative crystallinity, there is a slight departure from linearity. At the very earliest crystallization times, the double logarithmic plotting tends to exaggerate any error in the assignment of the crystallization starting time. From *Figure 3b* we see that a single Avrami exponent can describe cold crystallization of NEW-TPI over nearly the entire crystallization time, and thus a single mechanism or process governs isothermal cold crystallization from development of about 0.01–0.02 relative crystallinity until completion. The numerical values of n and K for all the isothermal crystallization temperatures are listed in *Table 1*. For crystallization temperatures below 330°C, we found that n is constant at about 3.5, and K increases as T_c increases. For T_c above 330°C, n decreases steadily from 3.5 to 2.8 as T_c increases to 360°C.

This represents the first report of isothermal crystallization kinetics for NEW-TPI. Here, we observed a single Avrami parameter n fit for the entire cold crystallization process. This behaviour has also been found in early work on isotactic poly(propylene) (iPP) melt crystallization[45–49], but more recent experiments indicate that there may exist secondary crystallization processes for iPP fractions[50]. Our value of Avrami exponent for cold crystallization of NEW-TPI is almost constant for all T_c below 330°C, which is the temperature at which NEW-TPI has its fastest cold crystallization rate, as indicated in *Figure 1*. An n value of 3, or 4, corresponds to three-dimensional growth and athermal, or thermal, nucleation, respectively[51]. However, our values of n for T_c below 330°C are all about 3.5, indicating a crystallization process between the athermal and thermal limiting cases. For crystallization temperatures above 330°C, n decreases from 3.5 to 2.8 as T_c increases from 330 to 360°C. Since we heat the sample from lower temperature up to T_c for the cold crystallization studies, it is possible for the amorphous polymer to form short-range ordered structure, which could serve as crystal seed nuclei as the temperature passes through the temperature of fastest crystallization (here 330°C). For cold crystallization above 330°C, the change to a lower Avrami exponent may indicate a change of mechanism to athermal heterogeneous nucleation, while for crystallization temperatures below 330°C thermal nucleation may be dominant.

We next use the Avrami rate constant, K, to gain additional insight into the isothermal crystallization process of NEW-TPI. We assume that the crystallization at high temperature follows the Hoffman–Lauritzen equation for secondary nucleation and heterogeneous formation of nuclei[52]. Then we can write the linear growth rate of crystals, G, as:

$$G = G_0 \exp[-U/R(T-T_\infty)] \exp(-K_g T_m^0/T\Delta T f) \quad (4)$$

where

$$K_g = pb\sigma\sigma_e/\Delta h k \quad (5)$$

In equation (4), U is the transport activation energy (using a suggested value of 6.28 kcal mol^{-1})[52], R is the universal gas constant, T_∞ is chosen to be $T_\infty = (T_g - 30)$ (ref. 52), T_m^0 is the infinite-crystal melting point, and ΔT is the degree of undercooling ($\Delta T = T_m - T$). The factor f ($f = 2T/(T + T_m^0)$) in the second exponential is a correction term to account for changes in Δh, the heat of fusion, with higher degrees of undercooling. The kinetic parameter, K_g, in equation (5) includes contributions from Δh, the side and fold surface free energies, σ and σ_e, respectively, the nucleus stem width, b, and Boltzmann's constant, k. The prefactor, p, in equation (5) is equal to 4 in crystal growth regimes I and III, and equal to 2 in regime II[52]. The kinetic parameter, K_g, is determined from plots of $\ln G + U/R(T-T_\infty)$ vs. $1/T\Delta T f$.

The linear growth rate is related to the overall crystallization kinetics parameter, K (see equation (3)), determined from the Avrami analysis according to $G \sim K^{1/n}$ where n is the Avrami exponent. K is also directly related to the crystallization half-time through equation (3) with $a = 0.5$. Therefore, in *Figure 3c*, to investigate the overall kinetics for NEW-TPI we have plotted $\ln(1/t_{1/2}) + U/R(T-T_\infty)$ vs. $1/T\Delta T f$. The plot shows two regions, indicating a break in slope at a crystallization temperature of 330°C. This is also the temperature at which we observe a change of Avrami parameter, n, from about 3.5 to 2.8. Although the data are not numerous, they do indicate a slope change from 1.84 to 3.77 giving a slope ratio of 2.05. The existence of two regions characterized by a factor of 2 slope ratio suggests a regime transition from regime II to III; and, within each regime of crystal growth, the linearity of this plot confirms the idea that heterogeneous nucleation and three-dimensional crystal growth models are appropriate for describing the kinetics of NEW-TPI.

The glass transition temperature

The glass transition temperature as a function of cold crystallization temperature is shown in *Figure 4a*. Glass transition temperatures for the semicrystalline samples range from 253 to 244°C, compared to a glass transition of 249°C for 100% amorphous NEW-TPI. The T_g values for semicrystalline NEW-TPI were found to decrease as T_c increases. We also found this to be the case in other polymers such as PPS[18,19,27] and PEEK[17,28]. However, there are two interesting differences in the T_g behaviour of NEW-TPI.

First, for crystallization temperatures at or below 330°C, T_g is equal to or greater than that of the purely amorphous sample, while for $T_c > 330$°C the value of T_g is smaller than that of purely amorphous NEW-TPI. This T_g determination is based upon the midpoint in the heat-capacity step. In the semicrystalline polymer, the range of the T_g step is quite broad and overlaps with the T_g range of the amorphous sample. Nonetheless, it is surprising that the midpoint determination for some semicrystalline NEW-TPI samples (crystallized above 330°C) should be below the amorphous T_g. This was not observed in our other studies of similar high-performance polymers PPS[18,19,27] and PEEK[17,28]. The distribution of relaxation times, indicated by the *breadth* of T_g region, is of course increased by cold crystallization, and additional evidence of the effect of crystallization temperature and time has been presented in our previous report, dealing with dielectric and mechanical relaxations in NEW-TPI[11,16].

Second, the shift to higher T_g seen in NEW-TPI crystallized below 330°C is very small, with T_g increasing

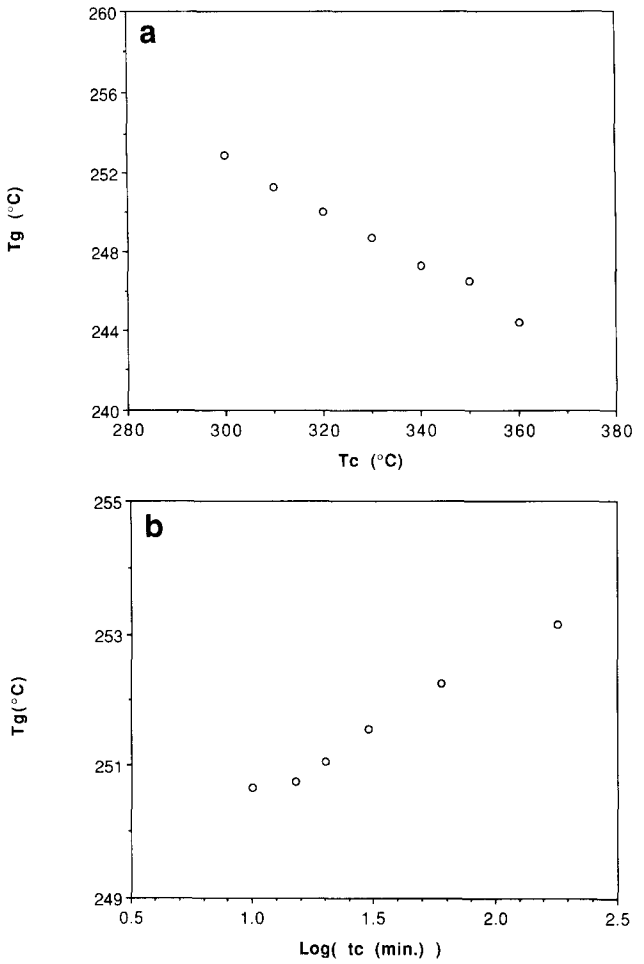

Figure 4 Glass transition temperature of NEW-TPI determined calorimetrically, as a function of (a) crystallization temperature and (b) crystallization time, at a scan rate of 10°C min^{-1}

by only about 4°C. It has generally been the case in other polymers we studied that the upward temperature shift was near 20–25°C after cold crystallization. The usual explanation for T_g shifting upwards is that there are constraints imposed on the amorphous phase by the crystals, which reduce the available configurations for the chains, and hence the mobility of the amorphous chains. When NEW-TPI crystallizes from the rubbery amorphous state, it does so with a minor effect on the glass transition temperature determined thermally, at least so far as the location of the midpoint in the T_g step is concerned.

As a comparison to the T_c dependence, we present the glass transition as a function of the crystallization *time* at 300°C in *Figure 4b*. The glass transition shows a minor but systematic change with the crystallization time, increasing from about 251 to 253°C as the crystallization time increases from 10 min to 3 h. By about 12 min, crystallization at 300°C is complete (see *Table 1*), therefore holding at longer times constitutes an annealing of the existing crystals. Compared with T_g of amorphous NEW-TPI, which is about 249°C, the T_g values of semicrystalline samples cold crystallized at 300°C for different times show a very slight increase.

Melting behaviour

Double melting peaks have been found for all cold crystallized NEW-TPI for T_c ranging from 300 to 360°C. The appearance of the endothermic scan is similar to cold crystallized PEEK or PPS, and we have previously shown examples of NEW-TPI scans[10], which will not be repeated here, for the sake of brevity. In *Figure 5* we show the melting peak temperatures T_{m1} and T_{m2} as functions of crystallization temperature (*Figure 5a*) or crystallization time (*Figure 5b*). In *Figure 5a*, the lower melting peak, T_{m1}, increases with T_c. The higher melting peak, T_{m2}, shows a minor decrease from 381 to 379°C as T_c increases from 300 to 320°C, then increases from 379 to 389°C as T_c increases from 330 to 360°C. From the extrapolation of the melting point vs. T_c curve to its intersection with the line $T_m = T_c$ (an approach that is strictly valid only for the case of isothermal melt crystallization[53]), we estimate the infinite-crystal melting point, T_m°. For NEW-TPI this estimate results in $T_m^\circ = 400$°C. Melt crystallization studies are currently under way[54] and will provide more information about the thermodynamic melting point.

In *Figure 5b*, we show the crystallization time dependence of the two melting peak positions during isothermal crystallization at 300°C. The low-temperature melting peak position increases from 312 to 319°C as the crystallization time increases from 10 min to 3 h. The peak position of the high-temperature peak decreases slightly from 380 to 378°C as a function of crystallization time. At 300°C, the upper and lower melting peaks are

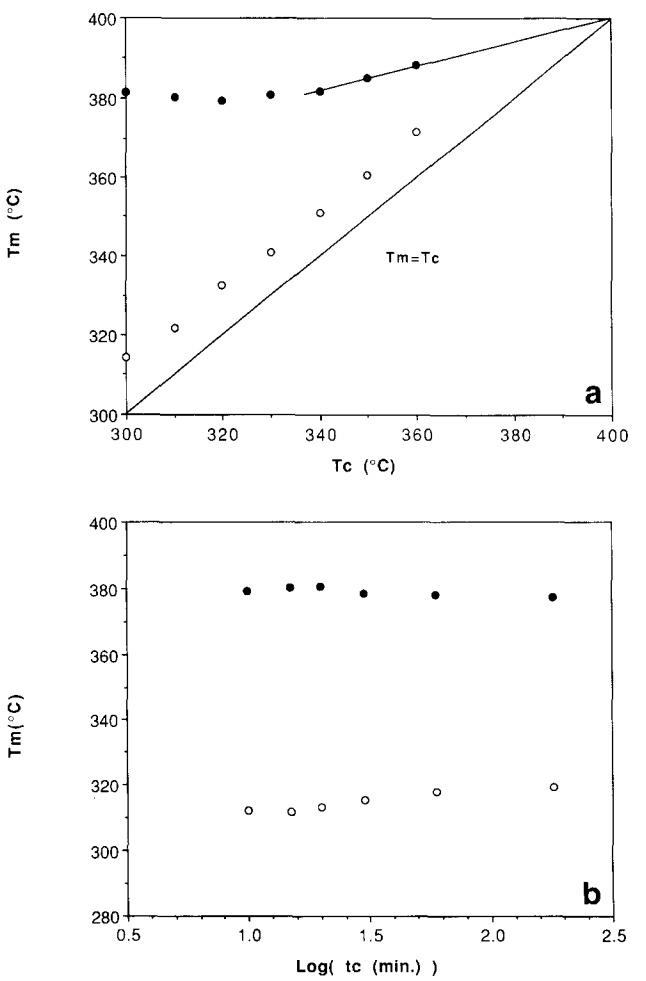

Figure 5 The lower melting peak temperature T_{m1} (○) and upper melting peak temperature T_{m2} (●) as a function of (a) crystallization temperature and (b) crystallization time at 300°C for NEW-TPI cold crystallization

easily separated into two distinct peaks. The endothermic peak area for the lower-temperature peak increases as t_c increases, while no clear trend is seen for the second endothermic area.

The double melting behaviour of cold crystallized NEW-TPI can be explained by the reorganization model, which we also used to describe melting of cold and melt crystallized PPS[40–42]. The first melting peak comes from the crystal population that exists in the sample at room temperature prior to the scan. These crystals were formed isothermally, but under high undercooling conditions of low chain mobility. These crystals are very imperfect and the most subject to reorganization. Just above the cold crystallization temperature, these imperfect crystals melt, forming the peak at T_{m1}, and become subject to recrystallization/reorganization, eventually melting again at T_{m2}. As the temperature is increased in the d.s.c. above T_{m1}, the reorganization rate will increase for those samples crystallized at $T_c < T'_c$ (i.e. at temperatures below the maximum in the growth-rate curve). For samples crystallized at $T_c > T'_c$ the reorganization/recrystallization rate will become progressively slower as temperature is increased above T_{m1}. The recrystallization/reorganization may occur without proceeding through a large-scale structural reorganization, but may proceed instead by continuous small-scale localized chain reorganization, and this may occur without a distinct exothermic heat flow peak between the two endotherms. Eventually as the temperature increases during the d.s.c. scan, the recrystallization rate decreases, and existing crystals will melt at T_{m2}.

In the case of melt crystallization, crystallization kinetics are considered to be dominated by nucleation at low degrees of undercooling, for temperatures well above the maximum in the growth rate vs. T_c curve. Melt crystallization kinetics are considered to be dominated by chain transport and viscosity contributions at higher degrees of undercooling, for example, at temperatures below T'_c (ref. 54). For the case of *cold* crystallization from the rubbery amorphous state, the crystallization kinetics would then most likely be dominated by chain transport in the temperature regime below T'_c. One question to consider is the manner in which cold crystallization kinetics should be treated as the isothermal crystallization temperature is increased above T'_c. In those polymers having faster crystal growth from the rubbery amorphous state, such as PET[29–33], PPS[37–42] and PEEK [34–36], it is not possible to heat the material above T'_c to the isothermal crystallization temperature without crystals already having been nucleated at lower temperature. In other words, cold crystallization at $T_c > T'_c$ really constitutes an annealing process in these polymers characterized by rapid cold crystallization kinetics.

However, in NEW-TPI the cold crystallization kinetics are relatively much slower and it is possible to heat NEW-TPI to $T_c > T'_c$ without observable crystallization taking place at a lower temperature. Thus, we expect that the cold crystallization of NEW-TPI below T'_c will be dominated by chain transport and viscosity; above $T'_c = 327°C$, crystallization may proceed by nucleation and growth of crystals at T_c from a condition of increased chain mobility. Unlike the other polymers mentioned above, cold crystallization of NEW-TPI above T'_c will not be simply an annealing process of crystals that had been nucleated at lower temperature.

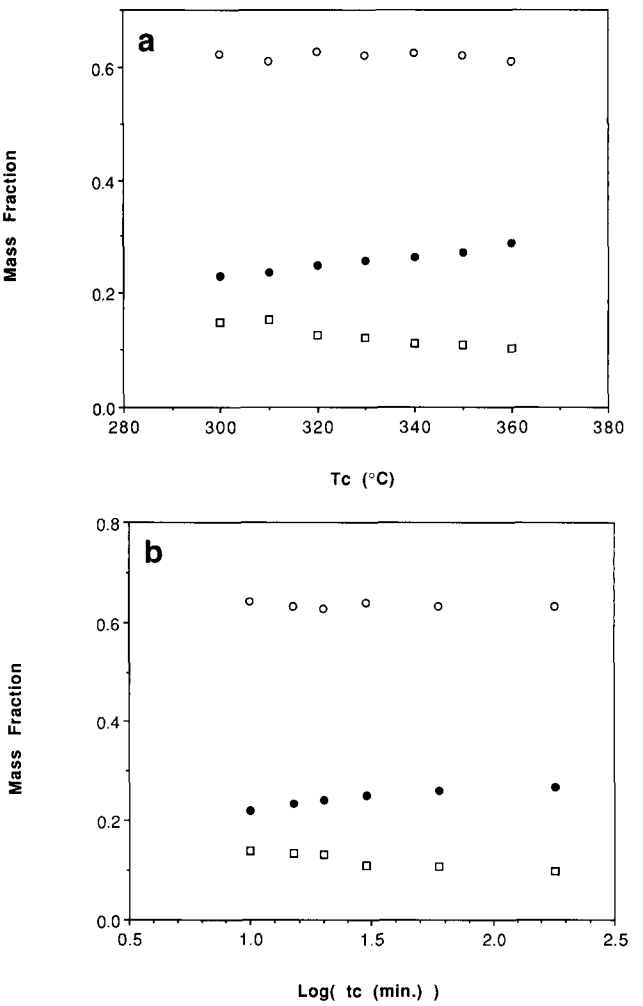

Figure 6 Crystalline (●), mobile amorphous (○) and rigid amorphous (□) mass fractions of NEW-TPI as a function of (a) crystallization temperature and (b) crystallization time at 300°C

Crystalline and amorphous fractions of NEW-TPI

The crystallinities of semicrystalline samples were obtained by calculating the ratio of their measured heat of fusion to that of 100% crystalline NEW-TPI, ΔH_{f0}, where $\Delta H_{f0} = 33.3 \text{ cal g}^{-1}$ (ref. 8). As indicated in *Figure 6a*, the mass fraction crystallinity, χ_c, ranges from 0.23 to 0.29 for T_c from 300 to 360°C. As with other high-performance polymers, NEW-TPI is not crystallizable to high extent. Depending on the crystallization temperature, 0.71–0.77 of NEW-TPI material is in the amorphous state (comprising both liquid-like and less-mobile, or rigid, amorphous components in the semicrystalline samples we prepared). Mass fraction crystallinity for isothermal cold crystallization at 300°C for different times is shown in *Figure 6b*. The crystallinity increases very rapidly in the first 10 min to 0.22 by weight, then it increases slowly to 0.28 as crystallization time increases.

The heat capacities below and above T_g were used to obtain the heat capacity at T_g by extrapolating to the midpoint of the glass transition region. The heat-capacity increment of a semicrystalline sample, $(\Delta C_p)_{sc}$, is considered to come only from the mobile amorphous portion, which becomes liquid within a narrow temperature range at T_g[20–28]. The fraction of liquid-like amorphous NEW-TPI, χ_a, was obtained by using the ratio of heat-capacity increment of the semicrystalline

sample to that of completely amorphous NEW-TPI at the glass transition temperature[20–28]. Here, the mobile or liquid-like amorphous phase undergoes a distinct heat-capacity jump, just as the purely amorphous sample does. The amount of liquid-like amorphous phase is shown by the open circles in *Figure 6a* for T_c dependence and *Figure 6b* for t_c dependence. We observed that the liquid-like amorphous phase is almost constant, about 0.62–0.63 irrespective of T_c or t_c.

The difference between total amorphous and liquid-like amorphous fractions is the rigid amorphous fraction, which is caused by the constraint of crystal lamellae on amorphous chains in the semicrystalline sample[20–28]. The rigid amorphous fraction has a smaller configurational entropy compared with the liquid-like amorphous fraction owing to the steric retardment of the crystals. The entropy difference is evidenced by the observation that the rigid amorphous chains experience no distinct heat-capacity change at the glass transition step associated with the most mobile amorphous fraction. In this regard, the rigid amorphous fraction behaves just as the crystal phase does. Of course, from the point of view of configurational entropy, we should expect a gradual change in entropy of the amorphous phase, ranging from that of the liquid-like amorphous chains to that of the rigid amorphous chains. (We would only expect distinctly different configurational entropy if the liquid-like and rigid amorphous fractions exist in completely different molecular environments, which is beyond the scope of this technique to address.) Nevertheless, the separation of different amorphous fractions is meaningful, since in the semicrystalline samples we still observe quite a sharp glass transition (distinct heat-capacity jump), though not as sharp as, and with a smaller heat-capacity increment than, that of the purely amorphous sample. This is an indication that there still exists a portion of liquid-like amorphous phase having a very narrow distribution of relaxation time, and it is relatively homogeneous compared with the rigid amorphous material.

The weight fraction of rigid amorphous chains is shown by the open squares in *Figures 6a* and *6b* and the values are listed in *Table 2*. The value of χ_{ra} decreases from 0.15 to 0.10 as T_c increases from 300 to 360°C, and has almost the same decrease as a function of increasing crystallization time. In contrast to the liquid-like amorphous phase, which has a narrow distribution of configurational entropy and a sharp transition in the heat capacity (the derivative of entropy with respect to temperature), the rigid amorphous fraction must have a very broad distribution of configurational entropy. Thus, we see no additional sharp step in heat capacity, i.e. we see no separate T_g for the rigid amorphous chains. Our prior dielectric relaxation results indicate that the rigid amorphous chains do relax above T_g of the liquid-like amorphous phase of NEW-TPI[11]. In terms of mobility, the liquid-like amorphous phase reaches the mobility of the liquid at its T_g, while the rigid material, because of its extremely heterogeneous nature, reaches the mobility of liquid little by little over a range of temperatures above T_g of the liquid-like amorphous phase.

The fraction of rigid amorphous material has been shown to be a very large weight fraction of material for some polymers such as PPS and PEEK[17–19,27,28]. In both these polymers, cold crystallization resulted in a very large rigid amorphous fraction, larger than that arising from either melt crystallization or slow cooling treatments. For example, it can be as much as 0.40 weight fraction in PPS cold crystallized at 150°C for 30 min. This PPS material has about the same degree of crystallinity as NEW-TPI, and therefore the amount of liquid-like amorphous phase (using equation (1)) is about 0.30. For the semicrystalline NEW-TPI, the liquid-like amorphous fraction is about 0.63–0.64 by weight, which is almost twice as large as that of PPS semicrystalline material having comparable crystallinity[18,19]. In NEW-TPI, the amount of rigid amorphous material is much smaller than in either PEEK or PPS, ranging from 0.15 to 0.10 dependent on the cold crystallization temperature and time. The amount of rigid amorphous phase is probably related both to the intrinsic stiffness of polymer chains and to the crystal morphology controlled by the crystallization kinetics. For example, a flexible polymer that crystallizes very rapidly may 'freeze' in large amounts of rigid amorphous phase. Such might be the case in poly(butylene terephthalate)[55–57]. On the other hand stiff-chain polymers may have highly entangled fold surfaces and crystal/amorphous interphase regions that lead to formation of rigid amorphous phase. The issues of chain flexibility and crystallization kinetics/morphology have so far not been investigated in a systematic way with regard to formation of rigid amorphous phase material, and this is likely to be an important area of future research.

Real-time SAXS

In *Figure 7*, we show the real-time small-angle X-ray scattering profiles of NEW-TPI during cold

Table 2 Crystalline, mobile amorphous and rigid amorphous fractions, glass transition temperatures, and melting peak temperatures[a] of NEW-TPI cold crystallized at the indicated temperatures

Crystallization temp. (°C)	χ_c (±0.01)	χ_a (±0.01)	χ_{ra} (±0.02)	T_g (°C) (±0.3°C)	T_{m1} (°C) (±0.3°C)	T_{m2} (°C) (±0.3°C)
300	0.23	0.62	0.15	252.9	314.4	381.5
310	0.24	0.61	0.15	251.3	321.9	380.3
320	0.25	0.62	0.13	250.0	332.5	379.5
330	0.26	0.62	0.12	248.7	340.9	380.9
340	0.26	0.63	0.11	247.3	351.0	381.9
350	0.27	0.62	0.11	246.5	360.5	385.0
360	0.29	0.61	0.10	244.4	371.8	389.4

[a] Values measured at d.s.c. scanning rate of 20°C min^{-1}

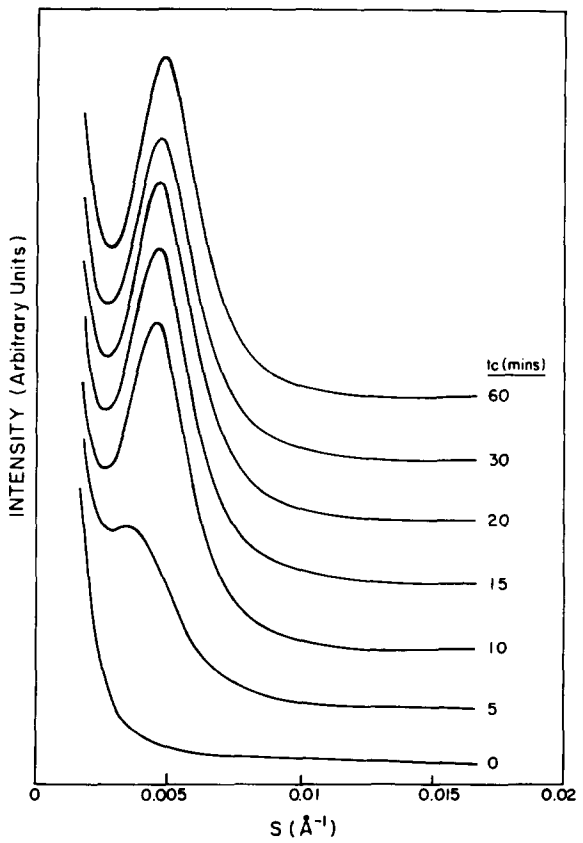

Figure 7 Real-time small-angle X-ray scattering intensity vs. scattering vector s, for NEW-TPI cold crystallized at 300°C for the times indicated

crystallization at 300°C. Before crystallization takes place, the SAXS pattern exhibits a typical single-phase pattern, showing a monotonic decrease from zero angle. At a crystallization time of 5 min, a shoulder appears at a scattering vector s ($s=2\sin\theta/\lambda$) of 0.005 Å^{-1}. For a crystallization time of 10 min, the shoulder becomes a very clear peak located at $s=0.006$ Å^{-1}. This indicates the formation of a periodic electron-density variation in the sample. As the crystallization time becomes longer than 15 min, the peak becomes sharper and intensity is stronger, but the peak position stays at almost the same scattering vector, implying an improvement of crystal stack alignment but no change of the average crystal stack long period. From the SAXS pattern, our estimated crystallization time at a cold crystallization temperature of 300°C is about 15 min, which is also quite consistent with the d.s.c. kinetics study. Lee and Phillips[58] suggest that the near-zero-angle intensity can be analysed to provide information about the distribution of crystallinity within a lamellar stack. Unfortunately, our data do not extend to sufficiently low angles to merit such an analysis. In addition, the cold crystallization process used here to crystallize NEW-TPI is likely to produce very imperfect crystals. The possibility of lamellar tilt within a stack of lamellae cannot be separated from crystallinity distribution within a stack, and this effect could be dominant. Therefore, we have not attempted the analysis of Lee and Phillips on our system.

For the real-time SAXS performed at 300°C, we observed significant change in the diffraction pattern intensity during the earliest 10 min of crystallization, because crystallinity increases rapidly during this period. But, we still see a steady change even after the first 10 min with SAXS intensity and peak resolution increasing, owing to the contribution of long-time annealing. At high temperatures like 300°C, long-time annealing of existing crystals will increase the difference in electron density even though the crystallinity measured by d.s.c. appears to increase very little. Annealing will result in smoothing of the crystal fold surface, removal of interior defects, and improvement in the lamellar alignment.

We assume that the lamellar structure of NEW-TPI consists of stacks of lamellae alternating with amorphous material. The one-dimensional electron-density correlation function, $K(z)$, is obtained by using:

$$K(z)=\int_0^\infty 4\pi I_{corr}(s)s^2\cos(2\pi sz)\,ds \qquad (6)$$

where z is a dimension along the normal to the lamellar stack[59,60]. Here, the intensity, $I_{corr}(s)$, is the intensity remaining after the background and thermal density fluctuations have been subtracted. The intensity vs. s data then were extrapolated to $s=0$ linearly. Also, Porod's law, $I(s)\sim s^{-4}$, was used to extrapolate the intensity data to $s=\infty$. In *Figure 8a*, we show a schematic plot of $K(z)$, and in *Figure 8b*, we show $K(z)$ vs. z at two annealing times of 5 and 60 min. Three morphological parameters, long period, lamellar thickness and crystallinity, are obtained according to the method described by Strobl and Schneider[60], which we review briefly in the next paragraph. More detail is available in the original work[60].

The method developed by Strobl and Schneider[60] extends the analysis of SAXS intensity profiles to systems in which: (1) the average long period may fluctuate,

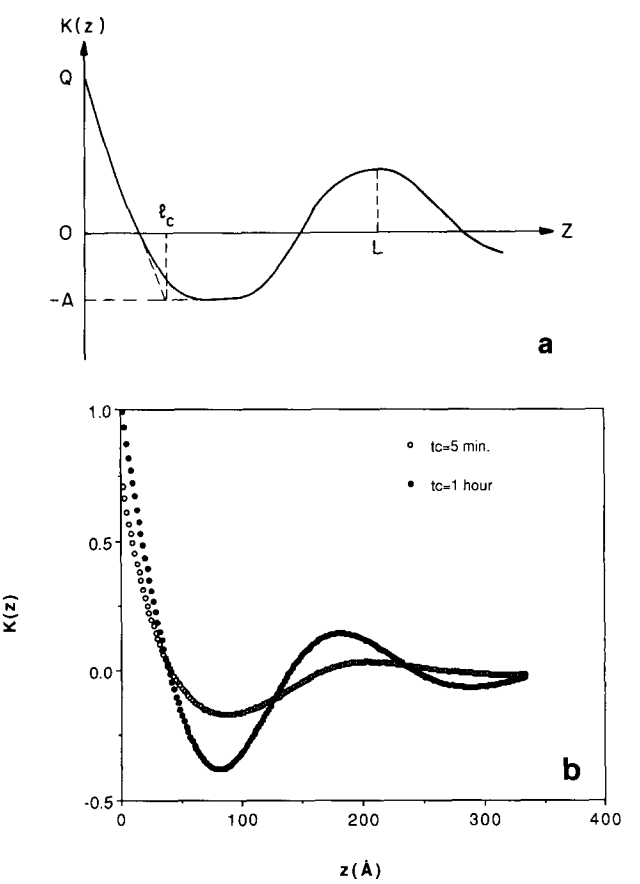

Figure 8 One-dimensional electron-density correlation function $K(z)$ vs. z: (a) schematic plot; (b) NEW-TPI crystallized at 300°C at different times

(2) the average lamellar thickness may fluctuate, and (3) the crystal and amorphous phases may be separated by a transition zone over which the electron density gradually changes. The method provides the ability to extract certain parameters of the system, including transition zone characteristics, from plots of the one-dimensional electron-density correlation function, $K(z)$, given by equation (6). A general plot of this function, in systems displaying such a transition zone, is shown in *Figure 8a*. From this figure we can immediately extract certain parameters including the average long period, invariant, crystallinity and average lamellar thickness. The average long period is the location of the first maximum of $K(z)$ for $z>0$, as shown by the location of L in *Figure 8a*. The invariant, $Q=\chi_c(1-\chi_c)(\rho_c-\rho_a)^2$, can be obtained by extrapolating the $K(z)$ vs. z curve at small z value to $z=0$. The horizontal line tangent to the first minimum of $K(z)$ vs. z is called the 'baseline'. Its coordinate is $-A$ where $A=\chi_c^2(\rho_c-\rho_a)^2$. The degree of crystallinity is then equal to the ratio $A/(A+Q)$. The average lamellar thickness is obtained as the z coordinate of the baseline intercept with the linear portion of $K(z)$ at small z values. From the $K(z)$ vs. z plot of our data, shown in *Figure 8b*, it is clear that, at $t_c=5$ min, the average long period is larger, the invariant is smaller, the crystallinity is smaller and the average lamellar thickness is smaller than those of the sample crystallized for $t_c=1$ h.

Figure 9a shows the long period (L) and lamellar thickness (l) as a function of annealing time at 300°C for all the samples we studied. The long period decreases, while the lamellar thickness increases, as annealing time increases. From annealing time 5 to 60 min, long period decreases from 203 to 180 Å, while lamellar thickness increases from 37 to 52 Å, which indicates that more crystal forms during long-time annealing. The c-axis repeat distance for NEW-TPI crystal lattice is about 25 Å[14]. Therefore the lamellar thickness, l, is roughly 1.5 to 2 times larger than the monomer length, implying very small average crystal thicknesses.

In *Figure 9b*, we present the degree of crystallinity as a function of annealing time at 300°C. The degree of crystallinity increases from 0 to 0.17 during the first 5 min, then reaches 0.26 at annealing time 15 min. Further increase of crystallinity, although very small, still appears as annealing time increases from 15 to 60 min. We should now comment on a limitation of the Strobl and Schneider analysis[60], which concerns the sensitivity of the analysis. The analysis is insensitive to systems in which the degree of crystallinity is close to 0.50, as can be seen from a consideration of Q, which changes weakly near $\chi_c=0.5$. In the present case, however, we have no limitation in applying this analysis because our polymer crystallinity is below 0.30. The lamellar thickness determined from a simple application of Bragg's law is equal to the product of the crystallinity and the long period. This simple calculation of l gives values within ± 1 Å of the values calculated from the one-dimensional electron-density correlation function analysis.

We make the simplifying assumption that the crystal and amorphous phase electron densities are independent of annealing time. Then the invariant, Q, can be obtained from the correlation function $K(z)$ as described above by using[60]:

$$Q=K(0) \tag{7a}$$

$$Q=\chi_c(1-\chi_c)(\rho_c-\rho_a)^2 \tag{7b}$$

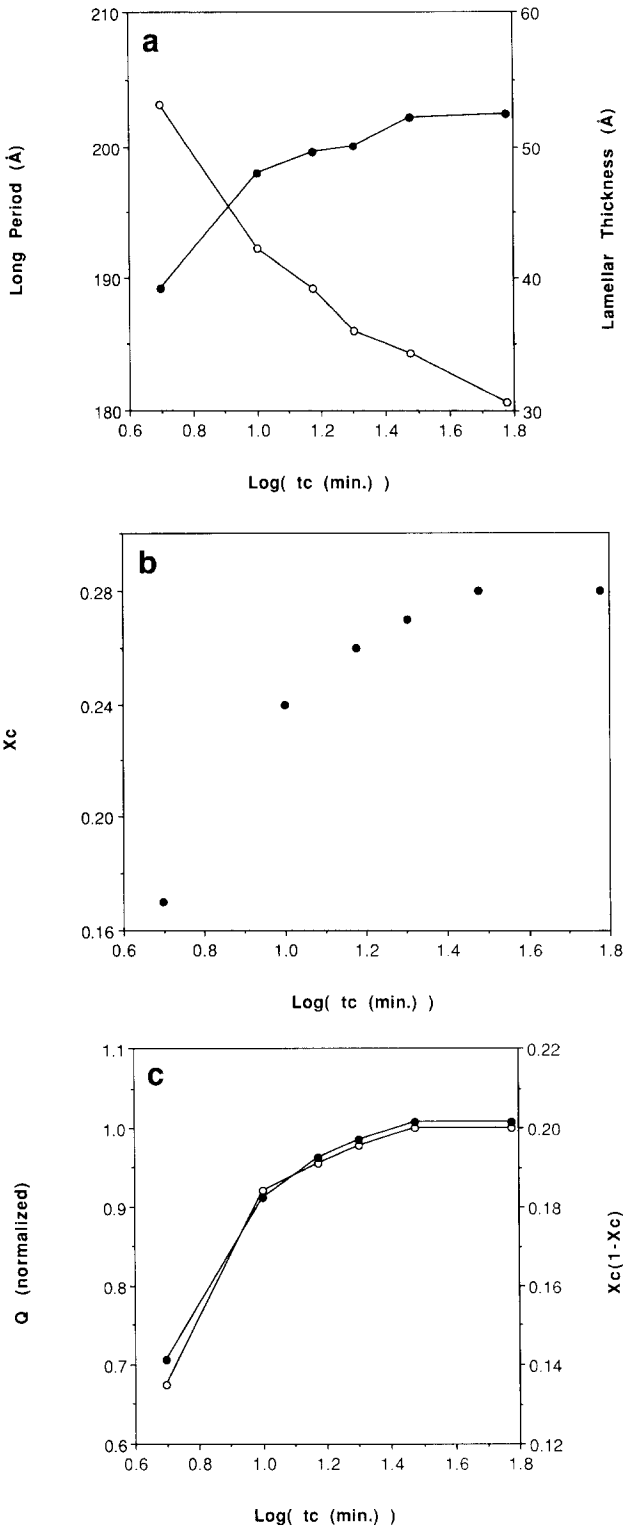

Figure 9 Morphological parameters obtained from SAXS analysis of NEW-TPI: (a) long period (○) and lamellar thickness (●), (b) volume crystallinity and (c) invariant Q (○) and $\chi_c(1-\chi_c)$ (●), vs. crystallization time at 300°C

where χ_c is the volume fraction of crystals, and ρ_c and ρ_a are the electron densities of the crystal and amorphous phases, respectively. From equation (7b), Q and $\chi_c(1-\chi_c)$ are then related by a constant. In *Figure 9c* we show the normalized Q obtained from equation (7a) and $\chi_c(1-\chi_c)$ from SAXS one-dimensional electron-density correlation function analysis. A scaling factor of 5 relates the two quantities shown in *Figure 9c*. Both Q and $\chi_c(1-\chi_c)$ increase as annealing time increases, and the normalized

values are quite comparable, indicating the consistency of the data obtained by the correlation function analysis.

The real-time SAXS analysis used to calculate the crystallinity vs. time (shown in *Figure 9b*) was performed on data taken at elevated temperature as crystallization progressed. These results for time development of absolute crystallinity can be compared to the crystallinity determined at room temperature, for samples treated at elevated temperature for the same times and then cooled. The latter values are shown in *Table 3*. After transferring the volume fraction of crystallinity from SAXS to mass fraction, we found that mass crystallinity obtained from SAXS is a little higher than from the thermal analysis (3% higher in mass fraction), yet they are still in reasonable agreement with each other.

The rigid amorphous fraction has been defined by thermal analysis[20–28], utilizing the rigidity of the molecular chain at the glass transition temperature. It represents material which, compared to the liquid-like amorphous phase, is constrained under the time/temperature conditions of normal d.s.c. scanning. It is not identically the same material as either the fold surface or the transition region over which chain flux is dissipated as chains emerge from the crystal surfaces, although it may be related to these regions. Certainly, all semicrystalline polymers with chain-folded lamellae have fold surfaces but many such polymers do not exhibit a rigid amorphous fraction from the standpoint of scanning thermal analysis of heat capacity. For methods that measure chain relaxation properties, such as dielectric or mechanical spectroscopies, the idea of an interphase may be broadened to encompass the fold surface, transition region for dissipation of chain flux, as well as interlamellar taut tie molecules and highly entangled amorphous material, which may be located farther away from the crystal stems.

Typically, SAXS has been used to probe the portion of the crystal/amorphous interphase that has an electron density intermediate between that of the perfect crystal and the completely amorphous material. To determine the size of the interphase region defined in this way, we used the corrected SAXS intensity. SAXS intensity at large s should follow Porod's law after subtracting the scattering from the thermal density fluctuations[61,62]. However, this is based on an assumption that the boundary between the crystal and amorphous phases is infinitely sharp. In the case of a very diffuse boundary, the corrected intensity at large s decreases more quickly,

Table 3 Crystalline, mobile amorphous and rigid amorphous mass fractions, and glass transition temperatures of NEW-TPI cold crystallized at 300°C for the indicated times

Crystallization time (min)	χ_c[a] (±0.01)	χ_a[a] (±0.01)	χ_{ra}[a] (±0.02)	T_g (°C)[a] (±0.3°C)	T_g (°C)[b] (±0.3°C)
0	0.00	1.00	0.00	248.8	281.0
10	0.22	0.64	0.14	250.7	284.0
15	0.23	0.63	0.14	250.8	n[c]
20	0.24	0.63	0.13	251.1	n
30	0.25	0.64	0.11	251.6	285.0
60	0.26	0.63	0.11	252.3	286.5
180	0.27	0.63	0.10	253.2	290.5

[a] Measured by using d.s.c. at scan rate of 20°C min^{-1}
[b] Measured by using dielectric loss maximum at 10 kHz
[c] Not tested under these conditions

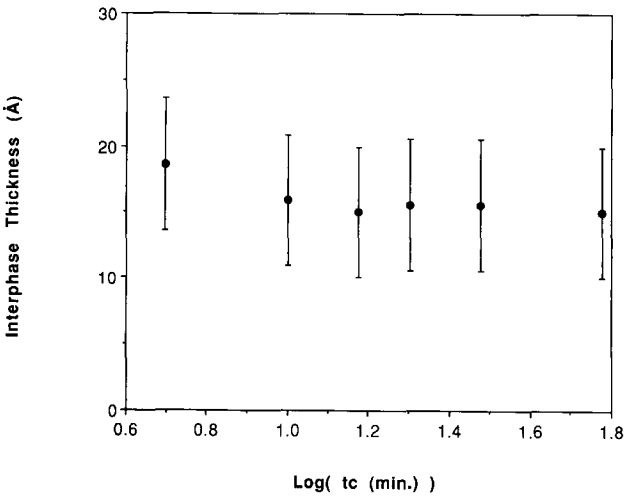

Figure 10 Interphase thickness of NEW-TPI as a function of crystallization time at 300°C

and is modelled as follows:

$$I_{corr}(s) = C \exp(-\pi^2 d^2 s^2)/s^4 \quad (8)$$

where $I_{corr}(s)$ is the intensity after subtraction of the thermal density fluctuation and d is the thickness of interphase, defined as above. Equation (8) holds only at large s. The relation can be described in an alternative way in which we write:

$$\ln[I_{corr}(s)s^4] = -\pi^2 d^2 s^2 + C \quad (9)$$

To obtain the interphase thickness, d, we plot $\ln[I_{corr}(s)s^4]$ vs. s^2. The scattering at large s is used to find the slope, $-\pi^2 d^2$. For t_c of 5 and 60 min, the slopes are -3500 and -2300 Å^2, indicating interphase thicknesses of 19 and 16 Å, respectively. In *Figure 10*, the interphase thicknesses at all the different annealing times are plotted. Within the accuracy of the data treatment, the interphase thicknesses are all the same, around 17 Å.

Two layers of interphase are included in one long period, and we can calculate the volume fraction of interphase material by using the ratio of twice d(interphase) to the long period, $2d/L$. Results indicate that, depending on the annealing time, there exists about 0.15–0.20 by volume of SAXS-determined interphase material in the annealed semicrystalline NEW-TPI. The volume fraction can be transferred to the weight fraction by using the density of crystal, mobile amorphous and interphase (assuming the density is between the crystal and mobile amorphous phase). The weight fraction of interphase is almost the same as the volume fraction. These values are close to the values we calculated from thermal analysis, which were about 0.10 to 0.15 by weight fraction. This is evidence that supports a view that rigid amorphous fraction in NEW-TPI is related to the interphase.

From our prior dielectric relaxation studies[11,17,18], and now from the standpoint of cold crystallization, we see that NEW-TPI has very different characteristics compared with some other high-performance thermoplastic polymers, like PPS and PEEK. NEW-TPI cold crystallization appears to proceed solely by a primary crystallization process, indicated by the fact that one Avrami parameter, n, fitted for nearly the whole crystallization time (as shown in *Figure 3b*). On the other hand for PPS[37–42] and PEEK[34–36], one Avrami

parameter could not be used over the entire crystallization range. In fact we showed that a very large portion, nearly 0.50 of the relative crystallinity, proceeds by secondary processes in the melt or cold crystallization of PEEK[35,36]. These secondary crystals should be located between the more perfect dominant crystals and the amorphous region. Constrained amorphous material may be created by the growth of secondary crystals and may also be located at the boundary between crystals. Therefore, it is tempting to suggest that there may be some relationship between the constrained interphase and the existence of imperfect secondary crystals. These imperfect crystals may provide the location, or base, for the formation of rigid amorphous chains. In PPS and PEEK, which have a large fraction of secondary crystallization, the fraction of rigid amorphous chains is also quite large, by weight as much as 0.40 for cold crystallized PPS and 0.35 for cold crystallized PEEK[17–19]. NEW-TPI cold crystallized samples, possibly owing to the lack of secondary crystals, or lack of bases for rigid amorphous chains, contain only about 0.10–0.15 of rigid amorphous material. In NEW-TPI, the small portion of interphase material detected independently by SAXS seems also to be related to its unique cold crystallization process.

CONCLUSIONS

The cold crystallization kinetics of NEW-TPI were studied as a function of crystallization temperature and time. A single Avrami exponent was found to describe the entire cold crystallization process nearly to the completion of crystallization. A regime II to III transition is seen over the range of cold crystallization temperatures we studied. From Avrami analysis, and from the linearity of the $\ln(t_{1/2}) + U/R(T - T_\infty)$ vs. $1/T\Delta Tf$ plots, we conclude that NEW-TPI cold crystallization proceeds via heterogeneous nucleation and three-dimensional crystal growth. Growth proceeds by a single primary process of crystallization, and little secondary crystallization is observed. The glass transition temperature is affected very little by the cold crystallization, increasing only a few degrees in the semicrystalline NEW-TPI. From this we conclude that crystals do not significantly shift the amorphous phase relaxation distribution compared to other high-performance polymers. Minimal constraint on the amorphous phase is also noted by the relatively small amount of rigid amorphous material, 0.10–0.15 by weight, identified through heat-capacity measurements. By using time-resolved SAXS, we have observed the crystal development with time during cold crystallization at 300°C. Both crystallinity and crystal perfection were found to increase during crystallization. The long period and lamellar thickness obtained from SAXS show a systematic dependence on the cold crystallization time. The crystals formed by isothermal cold crystallization are very small, with lamellar thicknesses ranging from about 1.5 to 2 times the monomer repeat unit.

ACKNOWLEDGEMENTS

Research was supported by the Petroleum Research Fund, administered by the American Chemical Society. The research was carried out in part at the National Synchrotron Light Source, Brookhaven National Laboratory. We thank Dr Alex Darovsky for assistance during our experiments at the Synchrotron.

REFERENCES

1 Scroog, C. E. *Macromol. Rev., J. Polym. Sci.* 1976, **2**, 161
2 Arnold, C. *Macromol. Rev., J. Polym. Sci.* 1979, **14**, 265
3 St Clair, A. K. and St Clair, T. L. in 'Polymers for High Technology, Electronics and Photonics' (Eds. M. J. Bowden and S. R. Turner), ACS Symp. Ser. 346, American Chemical Society, Washington DC, 1987, p. 437
4 Critchley, J. P., Knight, G. J. and Wright, W. W. 'Heat Resistant Polymers', Plenum Press, New York, 1986, p. 200
5 Hergenrother, P. M., Wakelyn, N. T. and Havens, S. J. *J. Polym. Sci.* 1987, **25**, 1093
6 Hergenrother, P. M. and Havens, S. J. *J. Polym. Sci.* 1989, **27**, 1161
7 Brekner, M. J. and Feger, C. *J. Polym. Sci.* 1987, **25**, 2005
8 Technical data sheet/A00, NEW-TPI, Mitsui-Toatsu Co.
9 Hou, T. H. and Reddy, J. M. *SAMPE Q.* 1991, **38** (January)
10 Friler, J. B. and Cebe, P. *Polym. Eng. Sci.* 1993, **33**, 587
11 Huo, P. and Cebe, P. *Polymer* 1993, **34**, 696
12 Sasuga, T. *Polymer* 1991, **32**, 1539
13 Hergenrother, P. M. SPE Conference on High Temperature Polymers and their Uses, Case Western Reserve University, 2–4 October, 1989
14 Sakaitani, H., Okuyama, K. and Arikawa, H. *Polym. Prepr. Japan* 1991, **40**, 478
15 Yuasa, S., Truji, M. and Takahashi, T. *Polym. Prepr. Japan* 1991, **40**, 491
16 Huo, P., Friler, J. B. and Cebe, P. *Mater. Res. Soc. Symp.* 1991, **227**, 239
17 Huo, P. and Cebe, P. *Macromolecules* 1992, **25**, 902
18 Huo, P. and Cebe, P. *J. Polym. Sci., Polym. Phys. Edn.* 1992, **30**, 239
19 Huo, P. and Cebe, P. *Colloid Polym. Sci.* 1992, **270**, 840
20 Suzuki, H., Grebowicz, J. and Wunderlich, B. *Makromol. Chem.* 1985, **186**, 1109
21 Loufakis, K. and Wunderlich, B. *Macromolecules* 1987, **20**, 2474
22 Gaur, U. and Wunderlich, B. *J. Phys. Chem. Ref. Data* 1981, **10**, 119
23 Wunderlich, B. and Czornyi, G. *Macromolecules* 1977, **10**, 906
24 Lau, S.-F. and Wunderlich, B. *J. Polym. Sci., Polym. Phys. Edn.* 1984, **22**, 379
25 Grebowicz, J., Lau, S. F. and Wunderlich, B. *J. Polym. Sci., Polym. Symp.* 1984, **71**, 19
26 Suzuki, H., Grebowicz, J. and Wunderlich, B. *Macromol. Chem.* 1985, **186**, 1109
27 Cheng, S. Z. D., Wu, Z. Q. and Wunderlich, B. *Macromolecules* 1987, **20**, 2802
28 Cheng, S. Z. D., Cao, M. Y. and Wunderlich, B. *Macromolecules* 1986, **19**, 1868
29 Vilanova, P. C., Ribas, S. M. and Guzman, G. M. *Polymer* 1985, **26**, 423
30 Palys, L. and Phillips, P. J. *J. Polym. Sci., Polym. Phys. Edn.* 1980, **18**, 829
31 Groeninckx, G., Reynaers, H., Berghmans, H. and Smets, G. *J. Polym. Sci., Polym. Phys. Edn.* 1980, **18**, 1311
32 Mayhan, K. G., James, W. J. and Bosch, W. *J. Appl. Polym. Sci.* 1965, **9**, 3605
33 Cobbs, W. H., Jr and Burton, R. L. *J. Polym. Sci.* 1952, **10**, 275
34 Lee, Y. and Porter, R. S. *Macromolecules* 1988, **21**, 2770
35 Cebe, P. and Hong, S.-D. *Polymer* 1986, **27**, 1183
36 Blundell, D. J. and Osborn, B. N. *Polymer* 1983, **24**, 953
37 Lovinger, A. J., Davis, D. D. and Padden, F. J., Jr *Polymer* 1985, **26**, 1595
38 Lopez, L. C. and Wilkes, G. L. *Polymer* 1988, **29**, 106
39 Lopez, L. C., Wilkes, G. L. and Geibel, J. F. *Polymer* 1989, **30**, 147
40 Chung, J. S. and Cebe, P. *J. Polym. Sci., Polym. Phys. Edn.* 1992, **30**, 163
41 Chung, J. S. and Cebe, P. *Polymer* 1992, **33**, 2312
42 Chung, J. S. and Cebe, P. *Polymer* 1992, **33**, 2325
43 Avrami, M. *J. Chem. Phys.* 1939, **7**, 1103
44 Avrami, M. *J. Chem. Phys.* 1940, **8**, 212
45 von Falkai, B. and Stuart, H. A. *Kolloid Z.* 1959, **162**, 138
46 von Falkai, B. *Makromol. Chem.* 1960, **41**, 86
47 Padden, F. J., Jr and Keith, H. D. *J. Appl. Phys.* 1959, **30**, 1479
48 Marker, L., Hay, P. M., Tilley, G. P., Early, R. M. and Sweeting, O. J. *J. Polym. Sci.* 1959, **38**, 33
49 Griffith, J. H. and Ranby, B. G. *J. Polym. Sci.* 1959, **38**, 107
50 Janimak, J. J., Cheng, S. Z. D., Zhang, A. and Hsieh, E. T. *Polymer* 1992, **33**, 728
51 Wunderlich, B. 'Macromolecular Physics', Academic Press, New York, 1980, Vol. 3

52 Hoffman, J. D., Davis, G. T. and Lauritzen, J. I. in 'Treatise on Solid State Chemistry' (Ed. N. B. Hannay), Plenum Press, New York, 1976
53 Hoffman, J. D. and Weeks, J. J. *J. Res. Natl. Bur. Stand.* 1962, **66**, 13
54 Rich, D., Huo, P., Lui, C. and Cebe, P. *Proc. Am. Chem. Soc. Div. Polym. Mater. Sci. Eng.* 1993, **68**, 124
55 Cheng, S. Z. D., Pan, R. and Wunderlich, B. *Makromol. Chem.* 1988, **189**, 2443
56 Huo, P. P., Cebe, P. and Capel, M. *J. Polym. Sci., Polym. Phys. Edn.* 1992, **30**, 1459
57 Huo, P. P., Cebe, P. and Capel, M. *Macromolecules* in press
58 Lee, Y. D., Phillips, P. J. and Lin, J. S. *J. Polym. Sci., Polym. Phys. Edn.* 1991, **29**, 1235
59 Glatter, O. and Kratky, O. 'Small Angle X-ray Scattering', Academic Press, New York, 1982
60 Strobl, G. R. and Schneider, M. *J. Polym. Sci., Polym. Phys. Edn.* 1980, **18**, 1343
61 Koberstein, J. T., Morra, B. and Stein, R. S. *J. Appl. Crystallogr.* 1980, **13**, 34
62 Russell, T. P., Ito, H. and Wignall, G. D. *Macromolecules* 1988, **21**, 1703